

Supplementary Materials for

Historical and future changes in global flood magnitude – Evidence from a model-observation investigation

Hong Xuan Do^{(1)(2)(3)(*)}, Fang Zhao^{(4)(5)(*)}, Seth Westra⁽¹⁾, Michael Leonard⁽¹⁾, Lukas Gudmundsson⁽⁶⁾, Julien Eric Stanislas Boulange⁽⁷⁾, Jinfeng Chang⁽⁸⁾, Philippe Ciais⁽⁸⁾, Dieter Gerten⁽⁵⁾⁽⁹⁾, Simon N. Gosling⁽¹⁰⁾, Hannes Müller Schmied⁽¹¹⁾⁽¹²⁾, Tobias Stacke⁽¹³⁾, Camelia-Eliza Telteu⁽¹¹⁾, Yoshihide Wada⁽¹⁴⁾.

(1) School of Civil, Environmental and Mining Engineering, University of Adelaide, Adelaide, Australia.

(2) Faculty of Environment and Natural Resources, Nong Lam University, Ho Chi Minh City, Vietnam.

(3) School for Environment and Sustainability, University of Michigan, Ann Arbor, Michigan, United States.

(4) School of Geographical Sciences, East China Normal University, Shanghai, China.

(5) Potsdam Institute for Climate Impact Research, Potsdam, Germany.

(6) Institute for Atmospheric and Climate Science, Department of Environmental Systems Science, ETH Zurich, Zurich, Switzerland.

(7) Center for Global Environmental Research, Japan.

(8) Laboratoire des Sciences du Climat et de l'Environnement, CEA-CNRS-UVSQ/IPSL, Université Paris Saclay, 91191 Gif sur Yvette, France.

(9) Geography Dept., Humboldt-Universität zu Berlin, Berlin, Germany.

(10) School of Geography, University of Nottingham, Nottingham, United Kingdom.

(11) Institute of Physical Geography, Goethe University Frankfurt, Frankfurt am Main, Germany.

(12) Senckenberg Leibniz Biodiversity and Climate Research Centre (SBiK-F), Frankfurt am Main, Germany.

(13) Institute of Coastal Research, Helmholtz-Zentrum Geesthacht (HZG), Geesthacht, Germany.

(14) International Institute for Applied Systems Analysis, Laxenburg, Austria.

(*) *Corresponding authors:* Hong Xuan Do (hong.do@adelaide.edu.au) and Fang Zhao (fangzhao@pik-potsdam.de)

Contents:

1. Brief information about the technical aspects of six global hydrological models that were used for this investigation.
2. Procedures to obtain simulated discharge at 3,666 locations considered in the model-comparison experiment.
3. Supplementary figure to demonstrate spatial uncertainty across ensemble members with different modelled atmospheric forcing.
4. Regional maps of Theil-Sen slope for historical trends in flood magnitude (MAX7 index) over North America, Europe, South America and Oceania.
5. Supplementary tables reporting trend characteristics introduced by each simulation at the global scale (the ensemble min/max/average were reported in the main text).

1 Simulation information

1.1 Simulation setting

This section summarises the key simulation settings of each global hydrological model (GHM). Note that more detailed information is available in the protocols of the Inter-Sectoral Impact Model Intercomparison Project (ISIMIP) available at <https://www.isimip.org/protocol>.

The following two input datasets were used for the GHM simulations, with specific model runs summarised in Table S1:

- 1. Climate & CO₂ concentration scenarios (i.e. atmospheric forcing)**
 - GSWP3: observations-based dataset providing the climate forcing data.
 - RCP2.6: future climate and CO₂ concentration from RCP2.6
 - RCP6.0: future climate and CO₂ concentration from RCP6.0
 - HINDCAST: historical modelled climate and CO₂ concentration.
- 2. Human influence and land-use scenarios**
 - nosoc: Naturalized runs (no human impact). No irrigation or man-made reservoirs. No population and GDP data prescribed.
 - varsoc: Varying historical land use and other human influences over historical period.
 - 2005soc: Fixed year-2005 land use and other human influences.

Note that GSWP3 was used as the sole observational atmospheric forcing dataset in this investigation. We also used modelled atmospheric forcing datasets introduced by four global climate models (GCM): GFDL-ESM2M, HadGEM2-ES, IPSL-CM5A-LR and MIROC5.

Table S1. Simulation set up of GHMs used in this investigation. ‘Climate’ represents atmospheric forcing dataset while ‘human’ represents human influence and land-use scenarios. Note that a more detailed inventory of available model runs is provided in Table S2.

Model	GSWP3_VARSOC	GSWP3_NOSOC	GCMHIND	GCMRCP2.6	GCMRCP6.0
H08	Climate: GSWP3 Human: varsoc	Climate: GSWP3 Human: nosoc	Climate: HINDCAST Human: 2005soc	Climate: rcp26 Human: 2005soc	Climate: RCP6.0 Human: 2005soc
LPJmL			Climate: HINDCAST Human: varsoc (except for ORCHIDEE using nosoc)		
PCR-GLOBWB					
WaterGAP2					
MPI-HM	Simulations not available				
ORCHIDEE					

The results of preliminary assessment over 3666 observation locations suggest minor influence of human influence and land-use scenarios on the characteristics of trends in streamflow extremes (see section 4 of this supplementary material), and thus only GSWP3_NOSOC was used in the main text (denoted as GSWP3 in the main text).

1.2 Similarities and differences among participated GHMs

Although “global hydrological models” (GHMs) has been used as a universal terminology to represent the participating models in this study, there are two groups of models with fundamental differences:

- Hydrological models (HMs): this group includes H08, MPI-HM, PCR-GLOBWB, and WaterGAP2, which focused on quantitatively simulate the water balance components such as streamflow.
- Dynamic global vegetation models (DGVMs): this group includes LPJmL and ORCHIDEE, which focused on the shifts in vegetation cycle under natural and anthropogenic factors.

Table S2 summarizes the differences in schematization across the models while the following paragraphs highlight the key differences. The information contained in this table was synthesized by the ISIMIP community. We noted that adapted versions of Table S2 have been used as Supplementary of two other manuscripts.

Generally, different models can potentially simulate the timing and magnitude of the streamflow differently due to their different structure, and the features that are included/excluded from the model schematization. Nevertheless, it is difficult to attribute discrepancy of simulated changes in streamflow indices for differences

in model schematization, as there is no study that has explored the influence of specific component on changes in streamflow indices. Below are some key differences across models.

Interception

H08 and MPI-HM models do not use an interception scheme. PCR-GLOBWB simulates canopy interception as a function of vegetation type, which is annually prescribed by HYDE, MIRCA, and GLOBCOVER datasets (ESA Globcover 2005 Project, led by MEDIAS-France/POSTEL). LPJmL, ORCHIDEE, and WaterGAP2 models take into consideration the leaf area index. Furthermore, DGVMs also take into consideration the CO₂ fertilization effect and the dynamic vegetation effects.

Snow

Four models (LPJmL, MPI-HM, PCR-GLOBWB, and WaterGAP2) use the degree-day method to simulate snow accumulation and melt, while H08 and ORCHIDEE models use the physically based energy balance method. The energy balance method generally determines lower snow water equivalent values than the degree-day method (Haddeland et al., 2011). However, H08 only consider a single snow layer, which means the model tend to produce abundant snowmelt sooner (relative to ORCHIDEE) when enough energy has been accumulated.

Soil profile and groundwater

Generally, HMs (H08, MPI-HM, PCR-GLOBWB, and WaterGAP2) have one or two soil layers, because they focused on matching observed and simulated streamflow rather than dynamic vegetation growth like DGVMs (which have six and eleven soil layers). Most HMs (except MPI-HM) have a single groundwater layer. LPJmL doesn't have a groundwater layer, but its seepage is considered to have the role of groundwater recharge and groundwater runoff.

Components determining surface runoff and river discharge

Predominantly, the surface runoff is modelled as saturation excess overland flow and subsurface runoff as a function of soil. The streamflow routing is made wherever possible but the approach varies across models such as linear reservoir cascade (MPI-HM and WaterGAP2), continuity equation derived from linear reservoir model (LPJmL), drainage direction map 30 minutes (H08), STN-30p river network (ORCHIDEE), travel time routing (characteristic distance) linked with dynamic reservoir management (PCR-GLOBWB). Other varying features that could lead to differences in simulated runoff as well as discharge are:

- Only MPI-HM and ORCHIDEE do not include the reservoir management.
- H08, LPJmL, and ORCHIDEE do not include lakes in their structure.
- H08 and LPJmL do not include wetland scheme in their structure.

Human water management

ORCHIDEE model does not simulate the water use sectors. Others models simulate, mainly, irrigation, but H08, PCR-GLOBWB, and WaterGAP2 also simulate differently water used in the domestic, industry and livestock sectors.

Table S2 Hydrological processes represented in the Global Hydrological Models included in the present study.

Models	Model version ISIMIP2a / ISIMIP2b	Interception scheme	CO ₂ fertilization effect	Snow scheme	Soil Layer / Total Soil Layer Depth (m)	Groundwater scheme	Surface runoff / subsurface runoff	Routing scheme	Reservoir operation	Lakes scheme	Wetlands scheme	Water use sectors scheme	References
H08	Hanasaki et al., (2008a&b) / Hanasaki et al., (2018)	no	no	energy balance method	1 / 1	1 renewable and 1 nonrenewable groundwater layer	saturation excess / $f(\text{soil})$ runoff properties varies with climate zones	based on 30° drainage direction map (DDM30)	yes	no	no	Irrigation, industry, domestic	Hanasaki et al., (2008a&b); Hanasaki et al., (2018).
LPJmL	Version 3.5 but with update of irrigation scheme in ISIMIP2b	$f(\text{LAI})$	yes	degree-day method with precipitation factor	6 / 13	seepage reported as groundwater recharge and groundwater runoff	saturation excess / $f(\text{soil})$	continuity equation derived from linear reservoir model	yes	no	no	irrigation	Bondeau et al., (2007) Schaphoff et al. (2013)
MPI-HM	R44 / v1.2	no	no	degree-day method	1 / 0 ¹	not included	saturation excess / $f(\text{soil})$	linear reservoir cascade	no	dynamical wetland extent scheme	dynamical wetland extent scheme	irrigation	Stacke and Hagemann, (2012)
ORCHIDEE	ORCHIDEE-Trunk Rev3013 / ORCHIDEE-MICT v8.4.1	$f(\text{LAI})$	yes	physically based snow module + energy balance method	11 / 2	1 groundwater layer	infiltration excess / $f(\text{soil})$	STN-30p river network	no	no	wetlands act as floodplains	no	Guimberteau et al., (2014) and Guimberteau et al., (2018)
PCR-GLOBWB	same version 2	$f(\text{veg})$	no	degree-day method	2 / 1.5	1 groundwater layer	saturation excess / $f(\text{soil})$ and gw	travel time routing (characteristic distance) linked with dynamic reservoir operation	yes	yes	columns of water (no soil)	irrigation, domestic, industry, livestock	Wada et al. (2014) Sutanudjaja et al., (2018)
WaterGAP2	2.2 / 2.2c	$f(\text{LAI})$	no	degree-day method	1 / Depending on land cover type between 0.1 and 4	1 groundwater layer	saturation excess, Beta function	linear reservoir cascade	yes	local and global lakes	local and global wetlands	irrigation, domestic, electricity, manufacturing, livestock	Müller Schmied et al., (2016)

Notes:

¹: MPI-HM defines the soil storage in terms of maximum water column, varying between 0 m and 5 m;

$f(\text{gw})$ = subsurface flow or interflow modelled as a function of groundwater; $f(\text{veg})$ = function of vegetation type;

$f(\text{soil})$ = subsurface flow or interflow modelled as a function of soil moisture (soil).

1.3 Model versions used in ISIMIP2a and ISIMIP2b

ISIMIP2a was designed as an evaluation framework to improve the models for the projection phase ISIMIP2b. As a result, the assessment using historical simulation (from 1971-2005) may not reflect the “true” capacity of the model used to simulate trends in floods during the future period (2006-2099). Specifically, PCR-GLOBWB is the only GHM that used the same version for both ISIMIP phases (noted in Figure S2). Below are the main modifications that have undertaken:

(1) LPJmL

The LPJmL model version used for ISIMIP2b was updated compared to the one used for ISIMIP2a in particular regarding the implementation of a new scheme to model irrigation systems, after Jägermeyr et al. (2015). In simulations with irrigation, this leads to various effects (differing in space and time) on most water balance components including discharge. Also the albedo of bare soil is made dependent on the soil moisture status.

(2) ORCHIDEE

ORCHIDEE-MICT v8.4.1 is a branch developed from ORCHIDEE-Trunk. ORCHIDEE-MICT improved the representation of the interactions between soil carbon, soil temperature and hydrology, and their resulting feedbacks on water and CO₂ fluxes at high latitude, in addition to a recently developed fire module (Guimberteau et al., 2018).

ORCHIDEE-MICT focusing on high-latitude phenomena include the following non-exhaustive series of pivotal hydrological and biogeochemical interactions.

- A representation of permafrost physics and seasonal freeze–thaw cycles, which determine the soil hydrologic and thermal budgets and the volume and timing of lateral water flows to rivers.
- The impact of winter snow acting as an insulating “barrier” between soils and overlying air from fall to early spring. These have subsequent effects on soil temperature and water content, feeding back onto snow thickness itself.
- The seasonal mediation of plant water availability via snowmelt water, transpiration losses and the depth of the permafrost table (active layer thickness), which in turn determine the availability of the lateral water flows that feed rivers in the warmer months.
- The limitations on plant productivity and biomass due to acute climatic conditions in high-latitude regions. These primarily involve biotically prohibitive cold temperatures from fall to late spring, low soil moisture in dry-summer regions, and fire events caused by hot and dry conditions.
- The buildup of large soil carbon stocks under cold conditions through the slow burial of organic matter in the permafrost via cryoturbation and sedimentary soil formation processes.
- Feedbacks between high soil carbon concentrations and profiles of soil temperature, water and permafrost carbon content.

(3) WaterGAP2

Modifications of water use models compared to model version in ISIMIP2a

Deficit irrigation with 70% of optimal irrigation was applied in grid cells, which were selected based on Döll et al. (2014) and have 1) groundwater depletion of $> 5 \text{ mm yr}^{-1}$ over 1989–2009 and 2) a $>5\%$ fraction of mean annual irrigation water withdrawals in total water withdrawals over 1989–2009.

Modifications of WaterGAP Global Hydrology Model compared to model version in ISIMIP2a

- Groundwater recharge below surface water bodies is enabled in semi-arid and arid regions.
- Dynamic land area fractions as consequence of dynamic surface water extents.
- Precipitation input on surface water bodies is now also multiplied with the evaporation reduction factor (as evaporation) to keep water balance consistent.
- Modified routing approach where water is routed through the storages dependent upon the fraction of surface water bodies; otherwise water is routed directly into the river.
- New total water capacity input based on Batjes (2012).

- For global lakes and reservoirs (where the water balance is calculated in the outflow cell), water demand of all riparian cells is included in the water balance of the outflow cell and thus can be satisfied by global lake or reservoir storage.
- All water storage equations in horizontal water balance are solved analytically (except for local lakes). Those equations now include net abstractions from surface water or groundwater. As a consequence, sequence of net abstractions has been changed to 1) global lakes or reservoirs, 2) rivers, 3) local lakes.
- Net cell runoff is strictly the difference between the outflow of a cell and inflow from upstream cells at the end of a time step.
- Area correction factor (CFA) is included in water balance of lakes and wetlands.
- In 2.2 (ISIMIP2a), local and global lake storage could vary between the maximum storage S_{\max} and zero. In 2.2c (as in versions before 2.2), local and global lake storage can drop to $-S_{\max}$ as described in Hunger and Döll (2008). The area reduction factor (corresponding to the evaporation reduction factor in Hunger and Döll (2008), their eq. 1) has been changed accordingly (denominator: $2 \times S_{\max}$). If lake storage S equals $-S_{\max}$, the reduction factor is 1; if S equals S_{\max} , the reduction factor is 0.
- Modified calibration routine: an uncertainty of 10% of long-term average river discharge is allowed (following Coxon et al., 2015), meaning that calibration runs in four steps: 1) test if γ alone is enough to calibrate to $\pm 1\%$ of observed value; 2) test if γ alone is enough to calibrate when 10% uncertainty of observed values are allowed; 3) adapt observed value by 10%, and test if γ plus CFA are sufficient for calibration; 4) add station correction factor (CFS) if all other steps were not successful, and set CFS values to 1 if between 0.98 and 1.02.
- All model parameters which are potentially used for the calibration/data assimilation integration (including also multipliers) are now read from a text file in Javascript Object Notation (JSON) format.
- Regional changes based on Döll et al. (2014): 1) for Mississippi Embayment Regional Aquifer, groundwater recharge was overestimated, and thus the fraction of runoff from land recharging groundwater was reduced from 80–90% to 10% in these cells; 2) groundwater depletion in the North China Plain was overestimated by a factor of 4, and thus runoff coefficient γ was reduced from 3–5 to 0.1 in this area; 3) all wetlands in Bangladesh were removed since diffuse groundwater recharge was unrealistically low.
- Due to different bug fixes reducing water balance error to a global sum of $< 1 \times 10^{-4} \text{ km}^3 \text{ yr}^{-1}$.
- In semi-arid/arid grid cells: In case of less precipitation than 12.5 mm day^{-1} , groundwater recharge is remaining in soil column (and not handled as runoff as in the version before).

(4) MPI-HM

The MPI-HM versions R44 and v1.2, as used in ISIMIP 2a and 2b respectively, differ only slightly in I/O infrastructure together with some modifications which concern only human impact simulations (which are not considered in ISIMIP 2a). More specifically changes are:

- Dynamic field allocation to allow for different model resolutions.
- Consistent reading and writing of parameter and restart files.
- Improvements for setup script.
- Limit irrigation gift to a maximum of 5% of the river flow storage per time step [1 day].
- Fix for parameter input (not affecting ISIMIP simulations).
- Fix for wetland water balance diagnostic (not affecting simulation results).

(5) H08

The newer version of the H08 model was used in ISIMIP2b (Hanasaki et al., 2018) while the older version used in ISIMIP2a (Hanasaki et al., 2008b). The main modifications of the updated version are:

- Revised irrigation/industrial and municipal water allocation.
- Inclusion of water transfer using aqueduct.
- Inclusion of seawater desalination scheme.
- Local reservoir implementation.

- Revised groundwater scheme.

Although the comparison between trends introduced by two versions of WaterGAP2 shows minor effects on changes in the key results of our investigation (see Section 3), simulations for other models are not readily available. As a result, the effect of modifications in GHMs cannot be checked in the context of this study.

2 Simulated streamflow extraction

For very large catchments, where excess rainfall takes a significant amount of time to reach the outlet, the routing scheme plays an important role in model performance related to high flow events (Zhao et al., 2017) and thus routed discharge is the more appropriate measure of simulated streamflow. The same simulation product, however, potentially does not perform well for small catchments, partially due to the coarse resolution of GHMs (Hunger and Döll, 2008). To address this concern, we adopted a common threshold of 9,000 km² (approximate the size of 1°×1° grid cell) to separate the selected catchments into two groups and applied different procedures to extract simulated streamflow.

2.1 Weighted-area average for stations with catchment from 0 to 9000 km²

2.1.1 Producing weighted-area tables

For stations with catchment area less than or equal to 9000 km², the catchment boundary was superimposed to the ISIMIP grid to identify intersecting cells, and a weighted-area table was calculated for each case. Simulated runoff was extracted by averaging the un-routed surface runoff from all intersect cells (considering weight). Runoff was then converted into discharge data.

Figure S1 provides an illustration of the weighted-area table for station US_0002282 (red dot; Merrill catchment of Pascagoula River, Mississippi, US) which has the total number of 15 upstream cells (dark-grey cells). Two components of the weighted-area table were used to label intersect cells: (1) cell number (dark red) and (2) normalised fraction of each cell (weights) that is covered by the catchment boundary (dark blue). The normalisation was performed such that the weights add up to one for each catchment, and these weights are used to extract simulated runoff for this catchment.

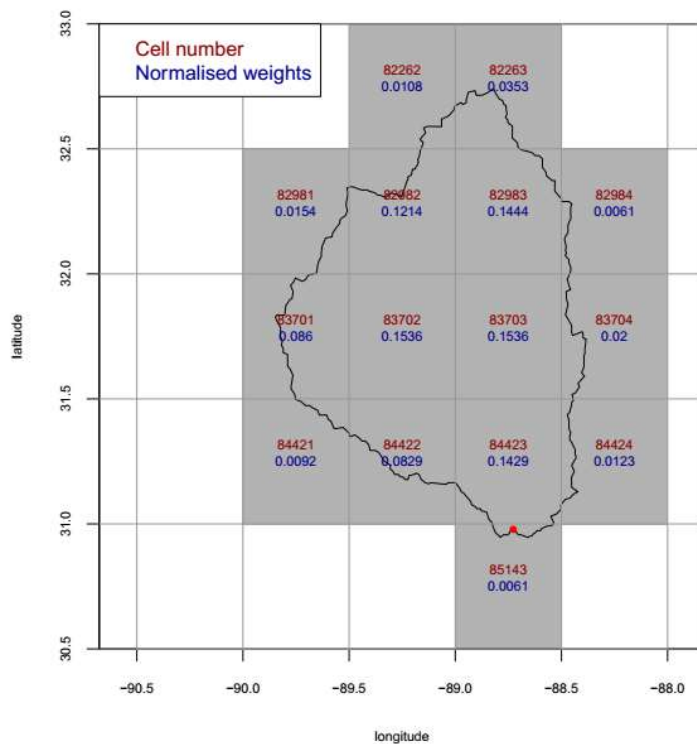
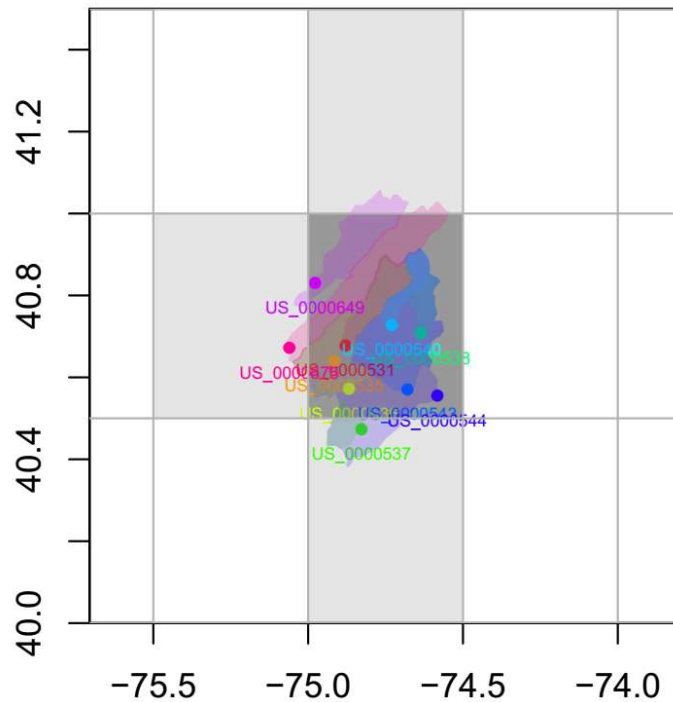


Figure S1. Illustration of the table of weights.

2.1.2 Averaging approach for cases where there were more than one catchment sharing similar weighted-area tables

Among catchments that have area less than 9000km², there are many instances where two or more catchments have (almost) identical simulated runoff as they have similar weighted-area tables. All ISIMIP models have a common assumption of uniform parameterisation for runoff generation in the 0.5×0.5 grid area, which in concept should represent an average value of runoff at finer resolution. Note that ORCHIDEE in ISIMIP2b (GCMs driven) was run at 1°×1° resolution, and the outputs were disaggregated evenly 0.5×0.5 resolution. Here we also treat catchments that intersect an identical set of dominant contributing grid-cells (total weights of at least 70%) as samples of an identical simulation domain. As a result, the area-weighted mean discharge of these catchments was calculated and used for model-observation comparison.

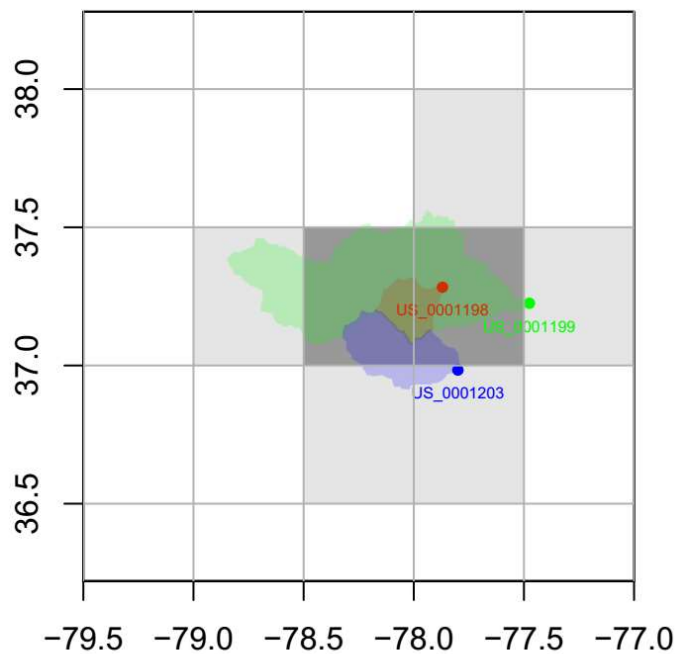
A search was conducted across all weighted-area tables to identify cases that have an identical set of intersecting cells contributing at least 70% to the total weighting. Figure S2 provides an example of these cases. In the top panel, boundaries of ten catchments were superimposed on top of the ISIMIP gridline (0.5×0.5 degree), demonstrating that they share a common cell (number 70051) which contributes at least 70% to the total weight (showed in the bottom panel).



70051	1	0.75	0.947	1	1	1	1	0.86	0.818	0.933
71491	0	0.25	0.053	0	0	0	0	0.018	0	0.067
70770	0	0	0	0	0	0	0	0.123	0	0
70771	0	0	0	0	0	0	0	0	0.182	0
US_0000531										
US_0000535										
US_0000536										
US_0000537										
US_0000538										
US_0000540										
US_0000543										
US_0000544										
US_0000649										
US_0000675										

Figure S2. Example of instances where there is a significant overlap in contributing cells. Top panel: locations of 10 catchments that share a common contributing grid-cell (cell number 70051 (in dark-grey colour) contributes at least 70% to the total weight of each catchment) although specific catchments have different contributing cells. Bottom panel: weighted-area table of these 10 catchments.

Figure S3 illustrates another case where three different catchments share two common cells (no. 76524 and 76525). These cells contribute 100%, 79.1%, and 76.4% to the weighted-area tables of catchment US_0001198, US_0001199, and US_0001203 respectively. In both examples, the identified catchments were considered samples of the same modeling domain.



76525	0.562	0.455	0.529
76524	0.438	0.336	0.235
75806	0	0.014	0
75803	0	0.189	0
75085	0	0.007	0
75805	0	0	0.147
75804	0	0	0.088
	US_0001198	US_0001199	US_0001203

Figure S3. Similar to Figure S2, but here we have two contributing cells. The total weight of these common cells (number 76524 and 76525, highlighted in dark-grey colour) is higher than 0.7 in all cases and thus these three catchments were considered samples of the same modelling domain.

For each set of n catchments with similar weighted-area tables, a single average discharge \bar{Q} (m³/s) was calculated to represent these individual time series in the model-observation comparison following below procedures:

For observed discharge:

1. Convert discharge Q (units: m³/s) to runoff rate R (units: m/day) using catchment area A (units: m²) for each catchment i .

$$R_i = Q_i \times 24 \times 3600 / A_i \quad (\text{m/day})$$

Average catchment size was also recorded:

$$\bar{A} = \frac{1}{n} \sum_{i=1}^n A_i \quad (\text{m}^2)$$

2. Average runoff rate across all catchments (considering area-weights)

$$\bar{R} = \frac{\sum_{i=1}^n R_i A_i}{\sum_{i=1}^n A_i} \quad (\text{m/day})$$

3. Back-calculate average discharge (m³/s):

$$\bar{Q} = \frac{\bar{R} \bar{A}}{24 \times 3600} \quad (\text{m}^3/\text{s})$$

For simulated discharge:

1. Extract runoff rate using weighted-area tables as described in Section 2.1 for all catchments.
2. Follow Step 2 and Step 3 of the observation procedure.

2.3 Discharge output identification for catchment with area greater than 9000 km²

For catchments with area greater than 9000km², the ‘discharge output’ approach was adopted to find GHM cells corresponding to the catchments following Zhao et al. (2017). For a specific catchment, the grid cell corresponding to the catchment outlet was identified by matching catchment area available in a 0.5° drainage direction map (DDM30 dataset, freely available at <http://www.uni->

frankfurt.de/45218101/DDM30) and the reported area. The identified grid cell was then used to extract simulated discharge available in the ISIMIP data repository. Stations were removed if the procedure could not identify any DDM30 grid cell surrounding the reported geographical location with a drainage area discrepancy less than 30% (see supplementary of Zhao et al. (2017) for detail).

3 Supplementary Figures

3.1 Capacity of GHMs to reproduce observed trends at continental scale

As stream gauges are not evenly distributed across the world, Figure S4 provides a zoomed-in map for four regions with relatively high number of stations (North America, Europe, South America, and Oceania). The most notable feature is a significantly lower strength of trends exhibited through GSWP3/GCMHIND ensemble average compared to GSIM observed trends. This pattern is likely the result of averaging technique (smoothed out variability of ensemble members) as the feature is more pronounced in GCMHIND (21 simulations) compared to GSWP3 (6 simulations). Visual inspection of these results suggests that the overall spatial pattern of observed trends seems to be preserved in GSWP3 while GCMHIND simulations tend to incorrectly simulate some spatial pattern of trends (e.g. over Oceania).



Figure S4. Normalised Theil-Sen slope for historical trends in flood magnitude (MAX7 index) over South America, Europe, South America and Oceania (left panels: GSIM; middle panels: GSWP3; right panels: GCMHIND). Multi-model average is shown for simulated trends. Trend is expressed in % change per decade.

Figure S5 illustrates the mean and standard deviation of simulated trends across all locations (% change per decade) for each individual ensemble member (multi-model average was showed in the manuscript). The mean and standard deviation of all trends (referred to as trend mean and trend standard deviation here-after) obtained from GSIM archive were also showed as dark blue line. GSWP3 simulations generally produced a higher trend mean and a lower trend standard deviation across all continents compared to the observed trends. The discrepancy varies substantially across different regions. For instance, Oceania

exhibited a discrepancy up to 7% per decade for the trend mean and 8% per decade for the trend standard deviation. This feature indicates a substantial inconsistency between simulated trends and observed trends. Among the six GHMs, ORCHIDEE, PCR-GLOBWB and WaterGAP2 tend to have a higher trend mean with the exception of Africa. This pattern potentially indicates the influence of either (i) parameterisation, (ii) model capacity in reproducing observed trend characteristics, or (iii) a bias of the GSWP3 forcing trends.

Figure S5 also shows relatively lower capacity of GCMHIND simulation in terms of reproducing observed trend mean and trend standard deviation in streamflow maxima. There is no clear ranking pattern in terms of the modelled atmospheric forcing being used, suggesting that uncertainty in GCM model was inherited differently across GHMs, likely due to the variation of parameterisation strategies.

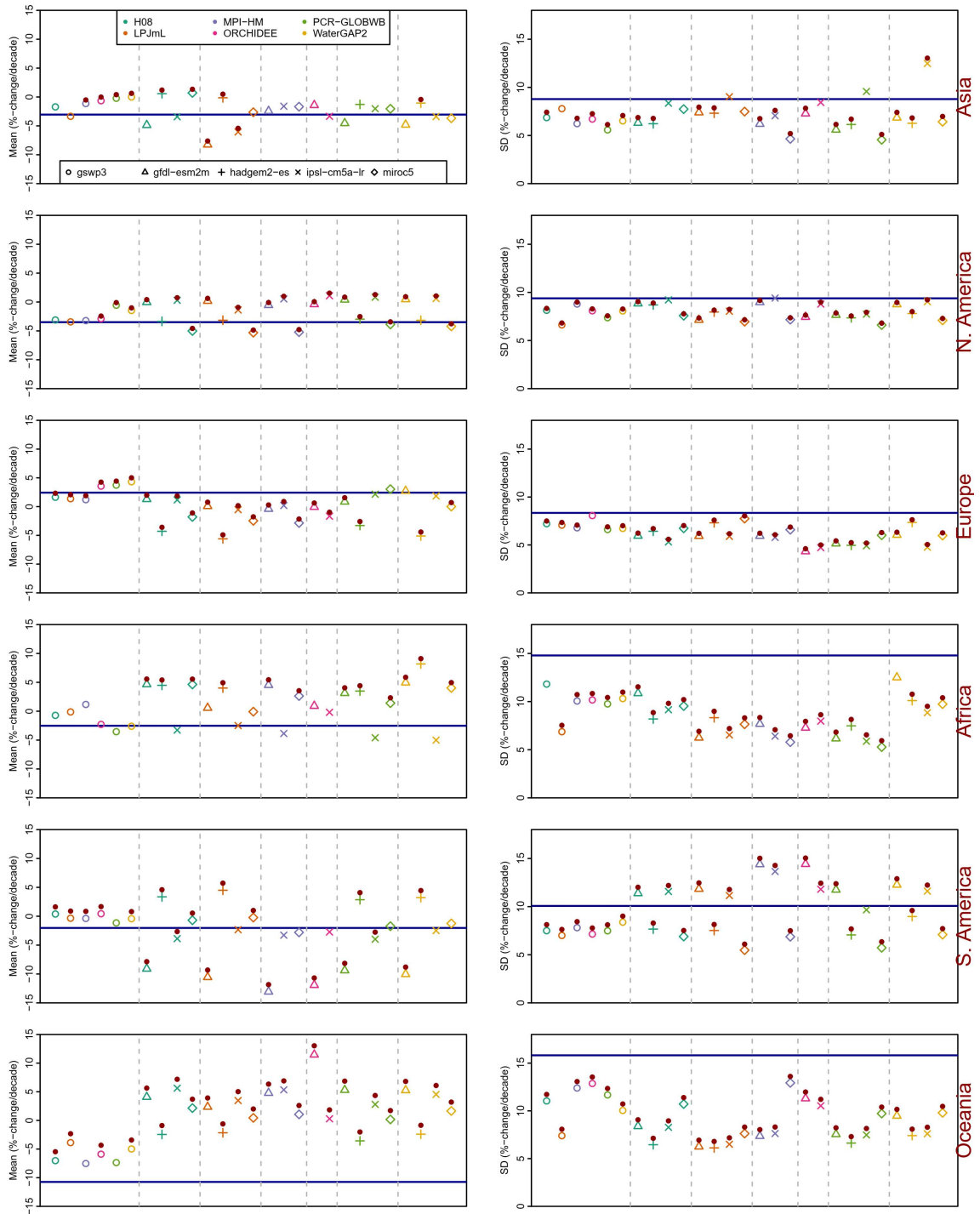


Figure S5. Mean (left panels) and standard deviation (right panels) of trends (% change per decade) exhibited from GSIM (horizontal blue line) observed trends and GSWP3/GCMHIND (hollow dots) simulated trends at the continental scale. The x-axis indicates different models. Note that y-axis range varies across panels. A null-hypothesis test was conducted to assess whether the mean/standard deviation of simulated trends is statistically different to that obtained from observed GSIM trends (horizontal blue line). Dark-red filled dots indicate simulations rejecting the null-hypothesis (i.e. which is that simulated trend mean/trend standard deviation is not statistically different to that obtained from GSIM).

3.2 Spatial uncertainty across simulated trends forced with different modelled atmospheric forcing

The assessment in section 3.3 of the main text suggests the combined GCM-GHM uncertainty has led to the presence of high uncertainty in terms of regions with significant projected trends in streamflow extremes. That is, a region could be projected by an overall increasing trend by one member and a decreasing trend by another member. This feature is illustrated in Figure S6, which shows a notable mismatch in the spatial structure of projected trends in MAX7 index between two ensemble members. Under the RCP2.6 greenhouse gas emission scenario, H08 forced with GFDL-ESM2M (top panels) projects an increasing trend for the majority of Australia and Siberia, while ORCHIDEE forced with IPSL-CM5A-LR (bottom panels) projects an overall decreasing trend for the same regions. This spatial uncertainty could come from either the climate trends introduced by GCMs (differentiate across GCMs), different RCPs, and model characteristics.

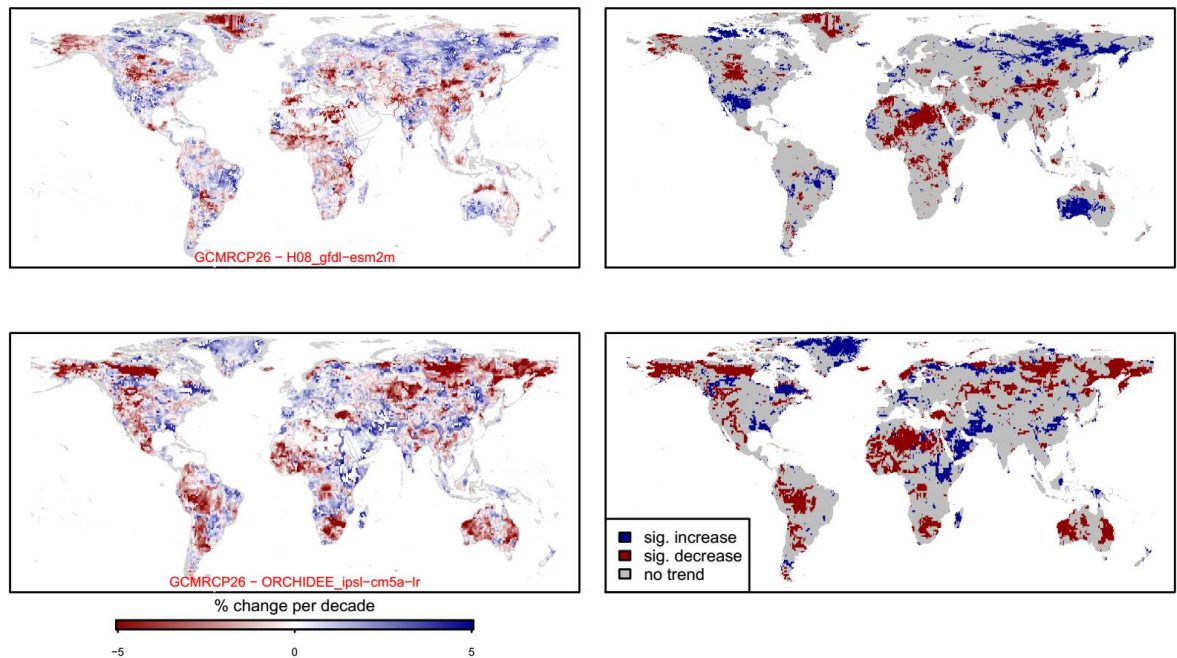


Figure S6. The magnitude (left panels) and significance (right panels) of trends in simulated MAX7 time series across all grid cells under RCP26 greenhouse gas emission scenario (2006-2099). Top panels: H08 forced with gfdl-esm2m climate data; bottom panels: ORCHIDEE forced with ipsl-cm5a-lr climate data. These two models had the lowest value of pattern similarity (correlation of -0.17).

3.3 Potential influence of model versions on detected trends

As mentioned in section 1.3 of this supplementary, there are changes in model versions that were used in two phases of ISIMIP. Specifically, ISIMIP2a was designed as an evaluation framework to improve the models for the projection phase ISIMIP2b. As a result, the assessment using historical simulation (from 1971-2005) may not reflect the “true” model capacity in simulating trends in floods during the future period (2006-2099).

While some models undergone minor changes (e.g., changes and bug-fixes done in MPI-HM affect only the human impact simulations – and the influence is insignificant), the different versions of the other models might lead to substantial differences of simulated trends. Within the context of this study, we managed to compare trends simulated by two versions of WaterGAP2 (Figure S7), and the influence of model versions to trends seem minor. However, not all simulations for the other models are readily available, thus the influence of model versions to the results cannot be explicitly identified in this study.

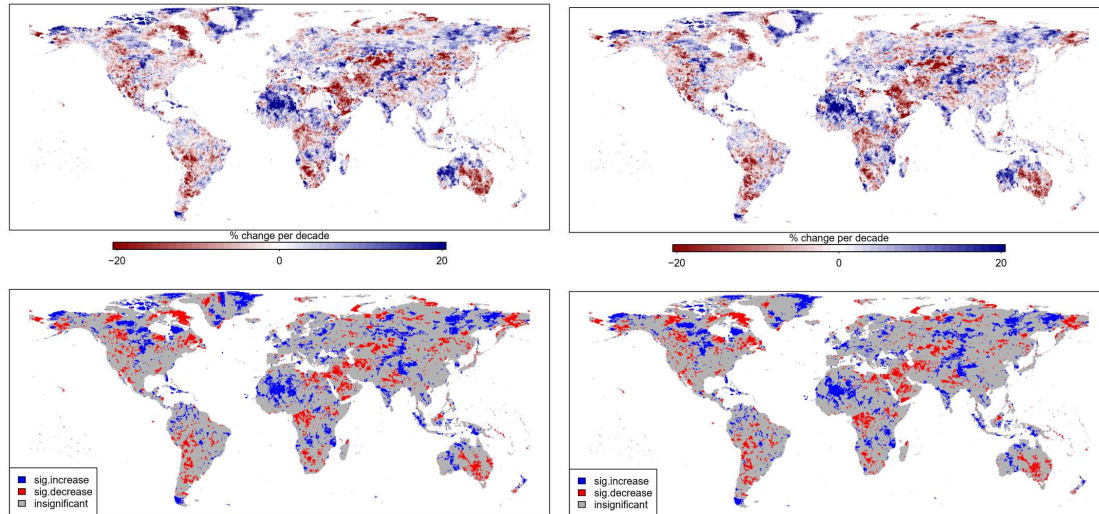


Figure S7. The magnitude (top panels) and significance (lower panels) of historical trends (1971-2005) in simulated MAX7 time series across all grid cells using two versions of WaterGAP. Left panels: WaterGAP2.2 (ISIMIP2a) which was used in ISIMIP2a; right panels: WaterGAP2.2c which was used in ISIMIP2b. Both simulations were forced with GSWP3 observed climate data.

4 Supplementary Tables

Considering a large number of simulations available (73 in total), the main text mostly used multi-model min/max/average to illustrate the results for cases where there is more than one simulation available for an identical GHM/spatial-domain. Table S2 provides a list of all 73 available models reported in this section together, with their simulation settings. Note that:

- (i) GSWP3_VARSOC simulations (listed in Table S2 as H08_GSWVAR, LPJ_GSWVAR, PCR_GSWVAR, and WAT_GSWVAR) were not reported in the main text as (1) there were only four simulations available (comparing to six simulations of GSWP3_NOSOC) and (2) the results obtained from GSWP3_NOSOC and GSWP3_VARSOC are similar (Table S3).
- (ii) In the main text, OBSHIS_NOSOC simulations were denoted as GSWP3.

Table S3. Available ISIMIP streamflow simulations and associated setting.

Seq	Streamflow simulations	GHM	Climate	Human	Period	
1.	H08_GSWVAR	H08	Observation (GSWPv3)	varsoc	1971-2005	
2.	H08_GSWNO		Observation (GSWPv3)	nosoc		
3.	H08_HIN_G		HINDCAST (GFDL-ESM2M)	2005soc		2006-2099
4.	H08_HIN_H		HINDCAST (HadGEM2-ES)			
5.	H08_HIN_I		HINDCAST (IPSL-CM5A-LR)			
6.	H08_HIN_M		HINDCAST (MIROC5)			
7.	H08_RCP2.6_G		RCP2.6 (GFDL-ESM2M)			
8.	H08_RCP2.6_H		RCP2.6 (HadGEM2-ES)		2005soc	
9.	H08_RCP2.6_I		RCP2.6 (IPSL-CM5A-LR)			
10.	H08_RCP2.6_M		RCP2.6 (MIROC5)			
11.	H08_RCP6.0_G		RCP6.0 (GFDL-ESM2M)			
12.	H08_RCP6.0_H		RCP6.0 (HadGEM2-ES)			

13.	H08_RCP6.0_I	LPJmL	RCP6.0 (IPSL-CM5A-LR)			
14.	H08_RCP6.0_M		RCP6.0 (MIROC5)			
15.	LPJ_GSWVAR		Observation (GSWPv3)	varsoc	1971-2005	
16.	LPJ_GSWNO		Observation (GSWPv3)	nosoc		
17.	LPJ_HIN_G		HINDCAST (GFDL-ESM2M)	varsoc		
18.	LPJ_HIN_H		HINDCAST (HadGEM2-ES)			
19.	LPJ_HIN_I		HINDCAST (IPSL-CM5A-LR)			
20.	LPJ_HIN_M		HINDCAST (MIROC5)			
21.	LPJ_RCP2.6_G		RCP2.6 (GFDL-ESM2M)	2005soc	2006-2099	
22.	LPJ_RCP2.6_H		RCP2.6 (HadGEM2-ES)			
23.	LPJ_RCP2.6_I		RCP2.6 (IPSL-CM5A-LR)			
24.	LPJ_RCP2.6_M		RCP2.6 (MIROC5)			
25.	LPJ_RCP6.0_G		RCP6.0 (GFDL-ESM2M)			
26.	LPJ_RCP6.0_H		RCP6.0 (HadGEM2-ES)			
27.	LPJ_RCP6.0_I		RCP6.0 (IPSL-CM5A-LR)			
28.	LPJ_RCP6.0_M		RCP6.0 (MIROC5)			
29.	MPI_GSWNO		MPI-HM	Observation (GSWPv3)	nosoc	1971-2005
30.	MPI_HIN_G			HINDCAST (GFDL-ESM2M)	varsoc	
31.	MPI_HIN_I	HINDCAST (IPSL-CM5A-LR)				
32.	MPI_HIN_M	HINDCAST (MIROC5)				
33.	MPI_RCP2.6_G	RCP2.6 (GFDL-ESM2M)		2005soc	2006-2099	
34.	MPI_RCP2.6_I	RCP2.6 (IPSL-CM5A-LR)				
35.	MPI_RCP2.6_M	RCP2.6 (MIROC5)				
36.	MPI_RCP6.0_G	RCP6.0 (GFDL-ESM2M)				
37.	MPI_RCP6.0_I	RCP6.0 (IPSL-CM5A-LR)				
38.	MPI_RCP6.0_M	RCP6.0 (MIROC5)				
39.	ORC_GSWNO	ORCHIDEE	Observation (GSWPv3)	nosoc	1971-2005	
40.	ORC_HIN_G		HINDCAST (GFDL-ESM2M)			
41.	ORC_HIN_I		HINDCAST (IPSL-CM5A-LR)			
42.	ORC_RCP2.6_G		RCP2.6 (GFDL-ESM2M)	nosoc (land use changes was considered)	2006-2099	
43.	ORC_RCP2.6_I		RCP2.6 (IPSL-CM5A-LR)			
44.	ORC_RCP6.0_G		RCP6.0 (GFDL-ESM2M)			
45.	ORC_RCP6.0_G		RCP6.0 (IPSL-CM5A-LR)			
46.	PCR_GSWVAR	PCR-GLOBWB	Observation (GSWPv3)	varsoc	1971-2005	
47.	PCR_GSWNO		Observation (GSWPv3)	nosoc		
48.	PCR_HIN_G		HINDCAST (GFDL-ESM2M)	varsoc		
49.	PCR_HIN_H		HINDCAST (HadGEM2-ES)			
50.	PCR_HIN_I		HINDCAST (IPSL-CM5A-LR)			
51.	PCR_HIN_M		HINDCAST (MIROC5)			
52.	PCR_RCP2.6_G		RCP2.6 (GFDL-ESM2M)	2005soc	2006-2099	
53.	PCR_RCP2.6_H		RCP2.6 (HadGEM2-ES)			
54.	PCR_RCP2.6_I		RCP2.6 (IPSL-CM5A-LR)			
55.	PCR_RCP2.6_M		RCP2.6 (MIROC5)			
56.	PCR_RCP6.0_G		RCP6.0 (GFDL-ESM2M)			
57.	PCR_RCP6.0_H		RCP6.0 (HadGEM2-ES)			
58.	PCR_RCP6.0_I		RCP6.0 (IPSL-CM5A-LR)			
59.	PCR_RCP6.0_M		RCP6.0 (MIROC5)			
60.	WAT_GSWVAR	WaterGAP2	Observation (GSWPv3)	varsoc	1971-2005	
61.	WAT_GSWNO		Observation (GSWPv3)	nosoc		
62.	WAT_HIN_G		HINDCAST (GFDL-ESM2M)	varsoc		
63.	WAT_HIN_H		HINDCAST (HadGEM2-ES)			
64.	WAT_HIN_I		HINDCAST (IPSL-CM5A-LR)			
65.	WAT_HIN_M		HINDCAST (MIROC5)			
66.	WAT_RCP2.6_G		RCP2.6 (GFDL-ESM2M)	2005soc	2006-2099	
67.	WAT_RCP2.6_H		RCP2.6 (HadGEM2-ES)			
68.	WAT_RCP2.6_I		RCP2.6 (IPSL-CM5A-LR)			

69.	WAT_RCP2.6_M		RCP2.6 (MIROC5)		
70.	WAT_RCP6.0_G		RCP6.0 (GFDL-ESM2M)		
71.	WAT_RCP6.0_H		RCP6.0 (HadGEM2-ES)		
72.	WAT_RCP6.0_I		RCP6.0 (IPSL-CM5A-LR)		
73.	WAT_RCP6.0_M		RCP6.0 (MIROC5)		

Most results of the main text only showed the multi-model average for GCMHIND simulations of each GHM (up to four simulations per GHM) (e.g. Table 3 of the main text, which presents the characteristics of trends in the MAX7 index over 1971-2005 period across 3666 locations globally). The following tables, therefore, provide the results of each experiment at the global scale for individual models to complement the key findings, in which:

- Table S3 (adapted from Table 2 in the main text) describe the hypothesis tests.
- Table S4 and S5 report trend mean/standard deviation, percentage of locations exhibiting significant trends and the correlation of simulated trends against observed trends (historical period from 1971 to 2005). The results of hypothesis test (described in Table S3) are also highlighted in Table S4 and Table S5.
- Tables S6 and S7 report the value of simulated trend mean/trend standard deviation and the percentage of cells exhibiting significant trends for future period (2006-2099). Note that the statistical test described in Table S3 was not adopted for these results.

As noted in the main text, trends in peak discharge exhibited from ‘naturalised runs’ (GSWP3_NOSOC) are similar to those obtained from ‘human impact runs’ (GSWP3_VARSOC). This is specifically illustrated through Table S4, in which the trends characteristic are quite similar between two settings. For instance, PCR_GSWVAR suggests a global trend mean (standard deviation) of 0.0 (7.7) % change per decade, with a spatial correlation against observed trends of 0.5. These results are very similar to that reported for PCR_GSWNO.

Table S4. Summary of the hypothesis tests conducted to address the first two objectives. The significance of these tests was reported in Table S4 and S5.

Objective	Null-Hypotheses	Streamflow dataset	Statistical tests
Objective 1: Capacity of GHMs to reproduce observed trends in flood hazards	Hypothesis 1: Trend means obtained from two streamflow datasets over observation locations were not statistically different from each other.		Two-sample t -test at the 10% two-sided significance level
	Hypothesis 2: Trend standard deviations obtained from two streamflow datasets over observation locations were not statistically different from each other.		Two-variance F -test at the 10% two-sided significance level
	Hypothesis 3: Percentage of significant trends obtained from all observation locations of a specific streamflow dataset was not produced by random chance.	(i) Observed discharge across 3,666 observation locations	Field significance test similar to that presented in Do et al. (2017) was adopted. A moving-block-bootstrap (block-length $L = 2$) was used to derive a null-hypothesis distribution of the change that occurred due to random chance. The null hypothesis is rejected at 5% one-sided significance level when the true percentage falls on the right-hand side of the 95 th percentile of the resampled distributions.
	Hypothesis 4: The correlation between trends obtained from two streamflow datasets was not significantly higher than '0' (i.e. zero pattern similarity).	(ii) Simulated discharge across 3,666 observation locations (extraction processes outlined in Section 2)	'Zero pattern similarity' was compared to the probability distribution function (PDF) of pairwise correlation between simulated and observed trends, drawn from a bootstrap procedure similar to that proposed by Kiktev et al. (2003). The null hypothesis is rejected at 5% one-sided significance level when zero correlation falls on the left-hand side of the 5th percentile of the resampled distributions.
	Hypothesis 5: The correlation between GCMHIND simulated trends and observed trends was not significantly lower than the correlation between GSWP3 simulated trends and observed trends		The actual pairwise correlation between GCMHIND simulated trends and observed trends (denoted by $r_{GCMHIND}$) was compared to the bootstrapped PDF of correlation exhibited from GSWP3 simulated trends (denoted by r_{GSWP}^*). If $r_{GCMHIND}$ falls on the left-hand side of the 5 th percentile r_{GSWP3}^* , there is evidence to reject the null-hypothesis at the 5% one-sided significance level.
Objective 2: The representativeness of observation locations in the GHM simulations	Hypothesis 6: Trend mean obtained from observation locations was not statistically different to that obtained from all grid cells.	(i) Simulated discharge across 3,666 observation locations (extraction processes outlined in Section 2)	Two-sample t -test at the 10% two-sided significance level
	Hypothesis 7: Trend standard deviation obtained from observation locations was not statistically different to that obtained from all grid cells.		Two-variance F -test at the 10% two-sided significance level

Hypothesis 8: Percentage of significant trends obtained from all grid cells of a specific streamflow dataset was not produced by random chance.	(ii) Routed discharge across all landmass grid cells (59,033 cells)	Field significance test similar to that presented in Hypothesis 3 but trends obtained from all grid cells were the subject of the assessment.
---	---	---

Table S5. Characteristics of trends in the MAX7 index (introduced by GHMs) over the 1971-2005 period averaged across the 3666 locations. Trend mean and trend standard deviation have units of %-change per decade. Gauge-based significant trends were identified using a Mann-Kendall test (10% two-sided significance level). The global significance of this result is then calculated using field significance test (5% one-sided significant level; highlighted in boldface text). Trend mean, trend standard deviation and trend spatial structure were compared against that exhibited by GSIM (see Hypothesis 1 to hypothesis 5 of Table S3 for description of hypothesis tests; significant values were represented in boldface text).

Streamflow simulations	Trend mean	Trend standard deviation	Percentages of significant		Correlation against observed trends
			Increasing trend	Decreasing trend	
H08_GSWVAR	-2.0	8.3	4.8	6.7	0.4
LPJ_GSWVAR	-2.6	7.5	4.6	9.2	0.4
PCR_GSWVAR	0.0	7.7	9.4	6.1	0.5
WAT_GSWVAR	-0.7	8.5	8.4	5.8	0.5
H08_GSWNO	-1.9	8.3	4.8	6.7	0.4
LPJ_GSWNO	-2.2	7.1	4.5	7.3	0.4
ORC_GSWNO	-1.4	8.6	7	8.2	0.4
MPI_GSWNO	-2.1	8.7	5.6	7.5	0.5
PCR_GSWNO	0.1	7.7	9.6	6.1	0.5
WAT_GSWNO	-0.3	8.2	8.5	4.2	0.5
H08_HIN_G	-0.4	8.9	6.1	7.8	0.1
H08_HIN_H	-2.8	8.4	2.2	10.8	-0.1
H08_HIN_I	0.1	8.9	7.7	4.4	0.0
H08_HIN_M	-3.6	7.8	3.4	12.0	0.1
LPJ_HIN_G	-0.8	8.0	6.3	8.3	0.1
LPJ_HIN_H	-2.9	8.1	2.8	14.6	0.0
LPJ_HIN_I	-1.3	8.0	4.1	10.1	0.1
LPJ_HIN_M	-4.1	7.3	3.5	17.3	0.2
ORC_HIN_G	-0.9	8.6	5.2	7.6	0.0
ORC_HIN_I	0.1	8.6	8.6	6.4	0.1
MPI_HIN_G	-1.3	9.5	5.9	7.9	0.1
MPI_HIN_I	0.2	9.2	8.8	5.6	0.0
MPI_HIN_M	-4.2	7.3	2.3	16.3	0.1
PCR_HIN_G	-0.2	8.0	8.3	9.0	0.1
PCR_HIN_H	-2.5	7.1	2.7	11.0	0.0
PCR_HIN_I	0.6	7.6	12.2	4.1	0.0
PCR_HIN_M	-2.1	7.0	6.9	13.5	0.1
WAT_HIN_G	0.2	9.2	8.2	5.6	0.1
WAT_HIN_H	-2.9	8.1	2.7	10.9	-0.1
WAT_HIN_I	0.5	8.8	6.2	4.2	-0.1
WAT_HIN_M	-2.9	7.3	4.3	11.4	0.1

Table S6. Trend mean, trend standard deviation and percentage of significant trends averaged across all simulation grid cells. Trend mean and trend standard deviation have units of %-change per decade. Cell-based significance was identified using the Mann-Kendall test at the 10% significance level. The global significance of this result is then calculated using field significance test at 5% one-sided level (highlighted in boldface text). Trend mean and trend standard deviation across all land mass were compared against that obtained across 3666 observation locations (reported in Table S4) and significant values are highlighted in boldface text (see Hypothesis 6 to hypothesis 8 of Table S3 for description of hypothesis tests).

Streamflow simulations	Trend mean	Trend standard deviation	Percentages of significant	
			Increasing trend	Decreasing trend
H08_GSWVAR	-0.5	10.1	8.4	10.7
LPJ_GSWVAR	-1.6	10.4	7.2	14.0
PCR_GSWVAR	-1.1	11.0	10.4	15.0
WAT_GSWVAR	-0.3	11.4	10.8	11.0
H08_GSWNO	-0.3	9.9	8.3	9.6
LPJ_GSWNO	-0.9	9.9	7.4	11.5
ORC_GSWNO	-0.9	9.6	6.1	7.8
MPI_GSWNO	-0.7	10.2	6.4	7.5
PCR_GSWNO	-1.0	10.9	10.7	14.7
WAT_GSWNO	0.0	11.1	10.9	10.1
H08_HIN_G	1.5	10.8	15.4	10.4
H08_HIN_H	0.0	8.5	7.4	9
H08_HIN_I	-0.7	9.3	7	10.7
H08_HIN_M	0.4	8.9	8.7	8
LPJ_HIN_G	-0.3	9.3	8.9	9.1
LPJ_HIN_H	-1.1	8.7	5.1	9.9
LPJ_HIN_I	-1.1	8.7	6.1	9.2
LPJ_HIN_M	-0.8	9.1	7.7	9.4
ORC_HIN_G	0.6	9.5	8.4	6.3
ORC_HIN_I	-0.9	8.2	3.9	6.8
MPI_HIN_G	-0.1	7.3	4.5	5
MPI_HIN_I	-0.2	10.3	10.9	11.2
MPI_HIN_M	-1.4	9.3	5.5	11.1
PCR_HIN_G	1.3	11.3	14.9	11.1
PCR_HIN_H	-0.4	8.7	8.1	10.5
PCR_HIN_I	-1.3	10.7	7.7	12.2
PCR_HIN_M	0.4	9	11.7	9.9
WAT_HIN_G	1.5	10.9	15.3	7.2
WAT_HIN_H	0.0	9.1	6.3	7.3
WAT_HIN_I	0.0	9.4	6.9	7.5
WAT_HIN_M	0.4	9.7	10.8	7.2

Table S7. Characteristics of projected trends (GCMRCP2.6) across 18 members at the global scale. Mean and standard deviation have unit of %-change per decade. Note that no statistical test was conducted.

Streamflow simulations	Trend mean	Trend standard deviation	Percentages of significant	
			Increasing trend	Decreasing trend
H08_RCP2.6_G	0.0	2.1	10.9	9.6
H08_RCP2.6_H	0.4	2.7	18.0	11.0
H08_RCP2.6_I	0.0	2.3	11.5	14.2
H08_RCP2.6_M	0.0	2.8	16.2	11.6
LPJ_RCP2.6_G	-0.1	1.8	7.5	7.4
LPJ_RCP2.6_H	0.0	2.1	10.7	10.6
LPJ_RCP2.6_I	-0.1	2.1	9.1	10.6
LPJ_RCP2.6_M	0.0	2.2	12.6	9.0
ORC_RCP2.6_G	-0.3	2.3	9.0	13.9
ORC_RCP2.6_I	-0.6	2.9	9.2	21.2
PCR_RCP2.6_G	0.1	2.1	11.0	9.0
PCR_RCP2.6_H	0.3	2.3	16.6	11.2
PCR_RCP2.6_I	0.0	2.8	15.5	13.9
PCR_RCP2.6_M	0.1	2.5	17.4	12.4
WAT_RCP2.6_G	0.0	2.1	9.6	7.1
WAT_RCP2.6_H	0.4	2.2	14.1	7.5
WAT_RCP2.6_I	0.2	2.3	12.3	10.0
WAT_RCP2.6_M	0.2	2.4	16.1	7.3

Table S8. Characteristics of projected trend (GCMRCP6.0) across 18 members at the global scale. Trend mean and trend standard deviation have unit of %-change per decade. Note that no statistical test was conducted.

Streamflow simulations	Trend mean	Trend standard deviation	Percentages of significant	
			Increasing trend	Decreasing trend
H08_RCP6.0_G	0.3	3.0	19.7	17.1
H08_RCP6.0_H	0.7	4.0	27.2	18
H08_RCP6.0_I	-0.4	3.4	15.3	27.1
H08_RCP6.0_M	0.4	3.3	26.2	14.9
LPJ_RCP6.0_G	-0.1	2.6	17.5	15.7
LPJ_RCP6.0_H	-0.2	3.4	22.3	21.9
LPJ_RCP6.0_I	-0.6	3.1	14.0	24.8
LPJ_RCP6.0_M	0.1	3.0	22.6	16.2
ORC_RCP6.0_G	-0.3	3.0	16.4	21.1
ORC_RCP6.0_I	-1.3	4.1	12.3	35.0
PCR_RCP6.0_G	-0.1	3.0	18.9	18.7
PCR_RCP6.0_H	0.1	3.8	26.0	22.2
PCR_RCP6.0_I	-0.5	3.6	18.3	25.6
PCR_RCP6.0_M	0.5	3.0	27.7	14.4
WAT_RCP6.0_G	0.4	2.6	23.5	9.8
WAT_RCP6.0_H	0.7	3.2	29.6	10.7
WAT_RCP6.0_I	0.0	3.2	20.4	16.9

WAT_RCP6.0_M	0.8	3.1	30.1	9.6
--------------	-----	-----	------	-----

Reference

Batjes, N. H.: ISRIC-WISE derived soil properties on a 5 by 5 arc-minutes global grid (ver. 1.2), ISRIC-World Soil Information, 2012.

Bondeau, A., Smith, P. C., Zaehle, S., Schaphoff, S., Lucht, W., Cramer, W., Gerten, D., LOTZE-CAMPEN, H., Müller, C., and Reichstein, M.: Modelling the role of agriculture for the 20th century global terrestrial carbon balance, *Global Change Biology*, 13, 679-706, 2007.

Coxon, G., Freer, J., Westerberg, I. K., Wagener, T., Woods, R., and Smith, P. J.: A novel framework for discharge uncertainty quantification applied to 500 UK gauging stations, *Water Resources Research*, 51, 5531-5546, 10.1002/2014wr016532, 2015.

Do, H. X., Westra, S., and Michael, L.: A global-scale investigation of trends in annual maximum streamflow, *Journal of Hydrology*, 10.1016/j.jhydrol.2017.06.015, 2017.

Döll, P., Müller Schmied, H., Schuh, C., Portmann, F. T., and Eicker, A.: Global-scale assessment of groundwater depletion and related groundwater abstractions: Combining hydrological modeling with information from well observations and GRACE satellites, *Water Resources Research*, 50, 5698-5720, 10.1002/2014wr015595, 2014.

Guimberteau, M., Ducharne, A., Ciais, P., Boisier, J.-P., Peng, S., De Weirtdt, M., and Verbeeck, H.: Testing conceptual and physically based soil hydrology schemes against observations for the Amazon Basin, 2014.

Guimberteau, M., Zhu, D., Maignan, F., Huang, Y., Yue, C., Dantec-Nédélec, S., Ottlé, C., Jornet-Puig, A., Bastos, A., Laurent, P., Goll, D., Bowring, S., Chang, J., Guenet, B., Tifafi, M., Peng, S., Krinner, G., Ducharne, A., Wang, F., Wang, T., Wang, X., Wang, Y., Yin, Z., Lauerwald, R., Joetzjer, E., Qiu, C., Kim, H., and Ciais, P.: ORCHIDEE-MICT (v8.4.1), a land surface model for the high latitudes: model description and validation, *Geosci. Model Dev.*, 11, 121-163, 10.5194/gmd-11-121-2018, 2018.

Hanasaki, N., Kanae, S., Oki, T., Masuda, K., Motoya, K., Shirakawa, N., Shen, Y., and Tanaka, K.: An integrated model for the assessment of global water resources – Part 2: Applications and assessments, *Hydrol. Earth Syst. Sci.*, 12, 1027-1037, 10.5194/hess-12-1027-2008, 2008a.

Hanasaki, N., Kanae, S., Oki, T., Masuda, K., Motoya, K., Shirakawa, N., Shen, Y., and Tanaka, K.: An integrated model for the assessment of global water resources – Part 1: Model description and input meteorological forcing, *Hydrol. Earth Syst. Sci.*, 12, 1007-1025, 10.5194/hess-12-1007-2008, 2008b.

Hanasaki, N., Yoshikawa, S., Pokhrel, Y., and Kanae, S.: A global hydrological simulation to specify the sources of water used by humans, *Hydrol. Earth Syst. Sci.*, 22, 789-817, 10.5194/hess-22-789-2018, 2018.

Hunger, M., and Döll, P.: Value of river discharge data for global-scale hydrological modeling, *Hydrology and Earth System Sciences Discussions*, 12, 841-861, 2008.

Jägermeyr, J., Gerten, D., Heinke, J., Schaphoff, S., Kumm, M., and Lucht, W.: Water savings potentials of irrigation systems: global simulation of processes and linkages, *Hydrol. Earth Syst. Sci.*, 19, 3073-3091, 10.5194/hess-19-3073-2015, 2015.

Mueller Schmied, H., Adam, L., Eisner, S., Fink, G., Flörke, M., Kim, H., Oki, T., Portmann, F. T., Reinecke, R., and Riedel, C.: Variations of global and continental water balance components as impacted by climate forcing uncertainty and human water use, *Hydrology and Earth System Sciences*, 20, 2877-2898, 2016.

Schaphoff, S., Heyder, U., Ostberg, S., Gerten, D., Heinke, J., and Lucht, W.: Contribution of permafrost soils to the global carbon budget, *Environmental Research Letters*, 8, 014026, 2013.

Stacke, T., and Hagemann, S.: Development and validation of a global dynamical wetlands extent scheme, *Hydrology and Earth System Science*, 16, 2915-2933, 2012.

Sutanudjaja, E. H., Van Beek, R., Wanders, N., Wada, Y., Bosmans, J. H., Drost, N., Van Der Ent, R. J., De Graaf, I. E., Hoch, J. M., and De Jong, K.: PCR-GLOBWB 2: a 5 arcmin global hydrological and water resources model, *Geoscientific Model Development*, 11, 2429-2453, 2018.

Wada, Y., Wissler, D., and Bierkens, M. F. P.: Global modeling of withdrawal, allocation and consumptive use of surface water and groundwater resources, *Earth Syst. Dynam.*, 5, 15-40, 10.5194/esd-5-15-2014, 2014.

Zhao, F., Veldkamp, T. I., Frieler, K., Schewe, J., Ostberg, S., Willner, S., Schauburger, B., Gosling, S. N., Schmied, H. M., and Portmann, F. T.: The critical role of the routing scheme in simulating peak river discharge in global hydrological models, *Environmental Research Letters*, 12, 075003, 2017.